Erik Jonsson School of Engineering and Computer Science

Tuning Electronic Transport in Epitaxial Graphene-Based Van Der Waals Heterostructures

Citation:

Lin, Yu-Chuan, Jun Li, Sergio,C. de la Barrera, Sarah M. Eichfeld, et al. 2016. "Tuning electronic transport in epitaxial graphene-based van der Waals heterostructures." Nanoscale 8, doi: 10.1039/C6NR01902A

Nanoscale

PAPER

View Article Online
View Journal | View Issue

Cite this: *Nanoscale*, 2016, **8**, 8947

Tuning electronic transport in epitaxial graphene-based van der Waals heterostructures†

Yu-Chuan Lin,[a] Jun Li,[b] Sergio C. de la Barrera,[b] Sarah M. Eichfeld,[a] Yifan Nie,[c] Rafik Addou,[c] Patrick C. Mende,[b] Robert M. Wallace,[c] Kyeongjae Cho,[c] Randall M. Feenstra[b] and Joshua A. Robinson*[a]

Received 9th March 2016,
Accepted 5th April 2016

DOI: 10.1039/c6nr01902a

www.rsc.org/nanoscale

Two-dimensional tungsten diselenide (WSe_2) has been used as a component in atomically thin photovoltaic devices, field effect transistors, and tunneling diodes in tandem with graphene. In some applications it is necessary to achieve efficient charge transport across the interface of layered WSe_2–graphene, a semiconductor to semimetal junction with a van der Waals (vdW) gap. In such cases, band alignment engineering is required to ensure a low-resistance, ohmic contact. In this work, we investigate the impact of graphene electronic properties on the transport at the WSe_2–graphene interface. Electrical transport measurements reveal a lower resistance between WSe_2 and fully hydrogenated epitaxial graphene (EG_{FH}) compared to WSe_2 grown on partially hydrogenated epitaxial graphene (EG_{PH}). Using low-energy electron microscopy and reflectivity on these samples, we extract the work function difference between the WSe_2 and graphene and employ a charge transfer model to determine the WSe_2 carrier density in both cases. The results indicate that WSe_2–EG_{FH} displays ohmic behavior at small biases due to a large hole density in the WSe_2, whereas WSe_2–EG_{PH} forms a Schottky barrier junction.

Introduction

Two-dimensional electronic materials such as monolayer semiconducting transition metal dichalcogenides (TMDs), phosphorene, and graphene have opened up new research fields because of their atomically thin nature, pristine surfaces, and unique optical and electrical properties.[1,2] While there are limitations in the properties that an individual 2D material can provide, combining various 2D materials into vdW heterostructures can produce structures that exhibit properties which are unattainable in their constituent materials (*i.e.* band-structure engineering).[3,4] There have been significant efforts on making manually-stacked vdW heterostructures with 2D layers exfoliated from bulk crystals.[2,3] For example, graphene-WS_2–graphene tunneling field effect transistors,[5] graphene-MoS_2–graphene heterojunction diodes,[6] and graphene-MoS_2 heterojunction phototransistors[7] all have been realized *via* mechanical exfoliation and stacking.

However, this process invariably produces interface contamination, such as physical adsorbates or defects introduced during the processing.[8] In order to obtain high-quality vdW heterostructures, powder vaporization (PV) and metal–organic chemical vapor deposition (MOCVD) techniques have been adapted for the direct synthesis of MoS_2, WSe_2, and GaSe on graphene.[9–13] Graphene is an ideal template for nucleation and growth of vdW heterostructures since many of the 2D crystals are isostructural.[10] In addition, its interesting characteristics such as high optical transparency, excellent flexibility, highly tunable carrier concentrations, and high in-plane ambipolar conductivity make it attractive as a transparent and flexible electrode.[14,15] Synthetic monolayer WSe_2 has been demonstrated as a tunneling barrier in the WSe_2–EG diodes.[11,16] However, large turn-on voltages (1.5 V–1.8 V) in the *I–V* characteristics of this vertical diode were observed, and tentatively attributed to the unfavorable n-type nature of the EG.[11] In this study, we demonstrate that the carrier type of the graphene is a critical parameter in controlling the charge transport at the TMD/graphene interface. Traditional mechanical transfer processes also utilized transferred graphene, which is inherently p-type due to water and environmental doping. These dopants ultimately control the electrical characteristics of the heterostructure stack. By controlling the doping type and concentration of EG from n- to p-*via in situ* hydrogen intercalation during the WSe_2 synthesis,[17] we demonstrate the origins of ohmic behavior in TMD/graphene structures, and

[a]*Department of Materials Science and Engineering and Center for 2-Dimensional and Layered Materials, The Pennsylvania State University, University Park, PA 16802, USA. E-mail: jrobinson@psu.edu*
[b]*Department of Physics, Carnegie Mellon University, Pittsburgh, PA 15213, USA*
[c]*Department of Materials Science and Engineering, The University of Texas at Dallas, Richardson, Texas 75080, USA*
†Electronic supplementary information (ESI) available. See DOI: 10.1039/c6nr01902a

obtain low resistance ohmic transport between a WSe_2 and graphene heterostructure. Low-energy electron microscopy, low-energy electron reflectivity, and conductive atomic force microscopy were performed on monolayer WSe_2–EG_{PH} and monolayer WSe_2–EG_{FH}, with the results showing that use of EG_{FH} (p-type graphene) as the bottom electrode of WSe_2–graphene diodes can lead to an Ohmic *I–V* behavior. Thus, EG_{FH} can serve as a high quality contact for heterostructures involving WSe_2 and additional 2D layers (located above the WSe_2).

Experimental

Epitaxial graphene was synthesized *via* silicon sublimation of the silicon face of 6H silicon carbide (6H SiC (0001)) at 1625 °C in a 200 Torr Ar environment inside a heating chamber made of pure graphite. The SiC substrates were pre-etched at 700 Torr with flowing 10% H_2/Ar mixtures (total 500 sccm) to remove subsurface damage due to substrate-polishing.[18] The WSe_2–EG growth is graphically illustrated in Fig. 1a.[16] The precursors chosen for WSe_2 synthesis are tungsten hexacarbonyl ($W(CO)_6$) and dimethylselenium ($(CH_3)_2Se$), which provide the W and Se, respectively. In order to eliminate carbon contamination from the precursor, a 100% H_2 environment is utilized for WSe_2 synthesis. This necessity of 100% H_2 significantly modulates the chemical environment of graphene, comparing to a dilute H_2 environment for WSe_2 growth. X-ray photoemission spectroscopy (XPS), equipped with a monochromatic Al-Kα source (E = 1486.7 eV) and an Omicron Argus detector operating with pass energy of 15 eV, carried out on the samples grown *via* PV using 5% H_2 at 900 °C and MOCVD using 100% H_2 at 800 °C, both in the same growth time, shows that the C 1s core level of the WSe_2–EG *via* MOCVD shifts towards a lower binding energy by 0.4 eV compared to that of WSe_2–EG grown *via* PV (Table S1†). This shift of C 1s core level in EG has been associated with hydrogen intercalation.[17,19] Evident from XPS, the 100% H_2 environment leads to complete hydrogen interaction at the EG/SiC interface, fully passivating the buffer at 900 °C.

The growth of WSe_2 on EG proceeds by vdW epitaxy, mediating the high lattice mismatch between WSe_2 and graphene.[20] Tungsten selenide (WSe_2) atomic layers are grown *via* MOCVD on EG/SiC substrates employing H_2 as a carrier gas[16] at 800 °C and 930 °C in order to study how hydrogen intercalation impacts the electrical transport between graphene and WSe_2, for the different growth temperatures (Fig. 1b). In order to eliminate carbon contamination in the WSe_2,[16] a 100% H_2 environment is utilized.

After 30 minutes growth, the as-grown atomic layers were confirmed to be monolayer WSe_2, 1 μm wide and 0.7 nm thick with atomic force microscopy (AFM) (Fig. 1c). The optical bandgap of monolayer WSe_2 measured *via* photoluminescence (PL) spectroscopy is found to be 1.63 eV (Fig. 2a), using a fitted Lorentzian peak function.[11,16] The Raman spectra exhibits two peaks of WSe_2 at 251 cm^{-1} and 260 cm^{-1} assigned to $E^1_{2g} + A_{1g}$ and 2LA, respectively (Inset, Fig. 2a).[16] The B^1_{2g} peak at 310 cm^{-1} typically seen in bi- and multilayer WSe_2 is absent, verifying the presence of a monolayer.[16,21]

Raman and PL measurements were performed in a WITec Confocal Raman microscope with a 488 nm wavelength laser. The topographic AFM micrographs were taken in a BRUKER.

Dimension with a scan rate of 1 Hz. The current-to-voltage (*I–V*) measurements performed on the samples were done in the same AFM with a PtIr-coated tip. Low-energy electron microscopy (LEEM) characterization was performed with an Elmitech III low-energy electron microscope. From sequences of images acquired with 0.1 eV energy spacing, Low-energy electron reflectivity (LEER) spectra were extracted at specific spatial locations on the surface.

Results and discussion

WSe_2 synthesis and buffer-layer decoupling

While crystal WSe_2 can be synthesized over a range of temperatures, the electrical properties of EG can be greatly modified at higher WSe_2 growth temperatures.[19] As-grown EG on SiC contains a C-rich "buffer layer" at the EC/SiC interface. The buffer

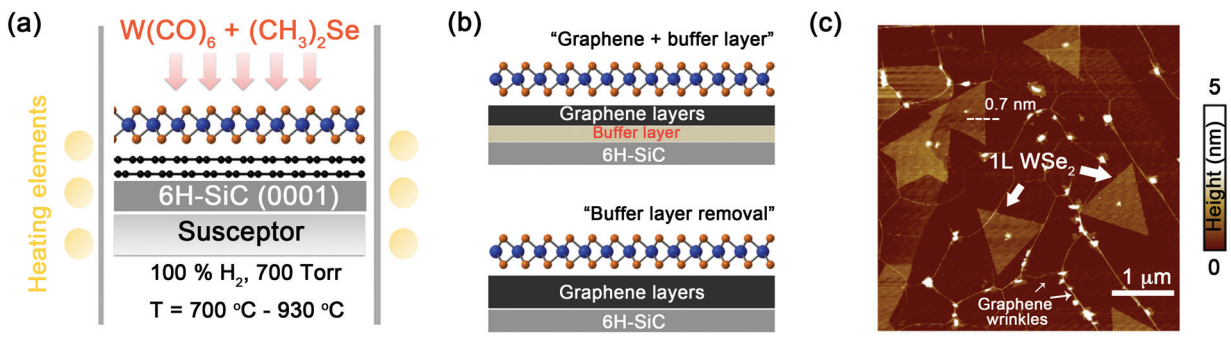

Fig. 1 (a) Illustration of MOCVD process of WSe_2 monolayer on EG-SiC and the synthesis conditions. (b) When the process of WSe_2 synthesis is carried out at a lower temperature the buffer layer decoupling is incomplete (top). A higher synthesis temperature can efficiently convert the buffer layer into a layer of graphene *via* hydrogen intercalation. (Bottom) (c) AFM image of WSe_2–EG heterostructure. Monolayers are mostly 0.7 nm in height. The wrinkles of graphene can be seen, which promoted vertical WSe_2 growth.

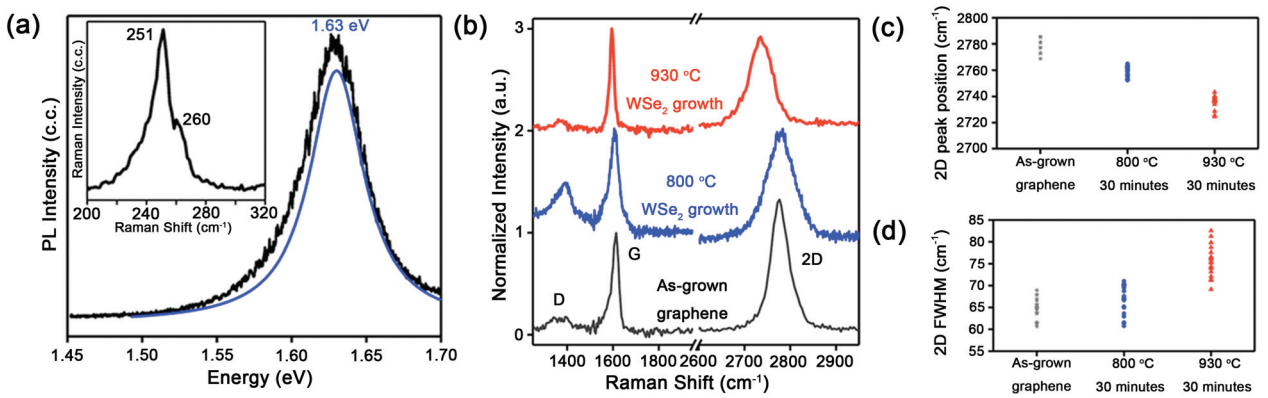

Fig. 2 (a) PL of the same samples in Fig. 1c emits at 1.63 eV corresponding to the optical bandgap of monolayer WSe_2. Inset in (c) is the Raman peaks of the same spot as PL. Peaks at 251 cm^{-1} and 260 cm^{-1} are assigned to $E^1_{2g}(\Gamma)/A_{1g}(\Gamma)$ and $A_{1g}(M)/2LA(M)$ of WSe_2 crystals, respectively.[16] (b) Higher growth temperature of WSe_2 can enhance the *in situ* hydrogenation on EG, evident by comparing Raman spectra of EG from 800 °C and 930 °C process. As-grown EG is present as reference. All of the spectrums were deconvoluted with SiC background. (c) and (d) Among the Raman 2D peak positions and corresponding FWHM from as-grown, 800 °C process and 930 °C process, the 930 °C process resulted in the largest position shift as well as width broadening, indicating increased graphene thickness and strain release due to the decoupling of buffer layers.

layer can subsequently be converted to a new layer of graphene by passivating the interface with hydrogen atoms, at elevated temperatures.[17,19] Furthermore, it has been demonstrated that the transformation of the buffer into an additional graphene layer is more efficient at a higher temperature when the hydrogenation time is fixed.[19] The EG Raman spectra (D, G, and 2D peaks)[22] before and after WSe_2 growth at 800 °C and 930 °C was compared to elucidate the impact of WSe_2 growth on structural properties of the EG (Fig. 2b). For the 800 °C, 30 minute growth of WSe_2, the D-peak intensity of EG increases as evidenced by a higher D/G ratio. This phenomenon can be interpreted as partial hydrogenation of the epitaxial graphene (EG_{PH}) that only converts a small portion of the buffer layer into graphene domains.[19,22] On the other hand, for the 930 °C, 30 minute WSe_2 growth, the D peak is suppressed and D/G ratio is notably smaller than those from the 800 °C process. This transformation of the D peak as the hydrogenation is increased is evidence of a more complete buffer elimination.[19] The Raman 2D peak of EG has been commonly used as an indicator for graphene thickness, graphene layer stacking, and a measure of compressive strain induced by graphene/SiC lattice mismatch.[23] In this work, the 2D peak of the 930 °C growth is at a relatively lower peak position, with broader full-width-half-maximum (FWHM), compared to that of the 800 °C growth. This is associated with a combination of increased layer thickness and released compressive strain.[19] This trend is evident (Fig. 2c and d) as an evolution of the peak position and FWHM of the 2D peak of graphene in as-grown (pre-WSe_2 growth), 800 °C WSe_2 growth, and 930 °C WSe_2 growth where data is accumulated in a 10 μm-line with an interval of 500 nm (total 20 spots). The as-grown samples have peak position and FWHM distributions of 2765–2782 cm^{-1} and 60–70 cm^{-1}, respectively. While the 800 °C growth only slightly shifts the distributions, the 930 °C growth leads to a shift of 40 cm^{-1} and an increase of 10 cm^{-1} in the 2D peak position and FWHM, respectively, indicating a complete transformation of the buffer layer to an additional EG layer. Additionally, the G peak (Fig. S1†) shifts towards a higher wavenumber by 3–5 cm^{-1} following the 930 °C growth, compared to as-grown graphene (1592.8 ± 3.5 cm^{-1}) and 800 °C WSe_2 growth (1593.5 ± 1.9 cm^{-1}). The shift of G peak has been associated with the doping effects on graphene, in which the wavenumber of the G peak increases when the Fermi energy of graphene moves away from the Dirac point towards both n- and p-type direction.[24] Since it has been reported that the buffer removal would move the Fermi energy to a point below the Dirac point,[25] the stiffening G peak of the EG from the 930 °C growth is hence contributed to a conversion from n-type to p-type graphene due to the buffer removal, as evident by the evolution of the 2D peak (Fig. 2c and d). Although the G peak provides information on the doping effects on graphene, the 2D peak has been chosen to be an effective indicator since its peak position has a larger shift than G peak in respond to hydrogenation/buffer removal.

LEEM/LEER measurements and analysis

In order to locally study the surface and electronic structure of the heterostructure samples, low-energy electron microscopy (LEEM) with electron energies of 0–20 eV is employed. In addition, low-energy electron reflectivity (LEER) spectra provides an accurate means of counting the number of graphene layers as well as extracting the work function variation over the surface.[26,27] The LEEM images of WSe_2–EG from 800 °C WSe_2 growth show triangular islands of WSe_2 with a characteristic size of 1 μm, nucleating preferentially near SiC step edge on the EG surface (Fig. 3a). The graphene is found predominantly in monolayer + buffer form, but small bi- and tri-layer graphene crystals are also found on the surface. This indicates that the buffer is nearly intact as-grown EG, or only a negligible portion of it has been eliminated during the 800 °C WSe_2 growth.

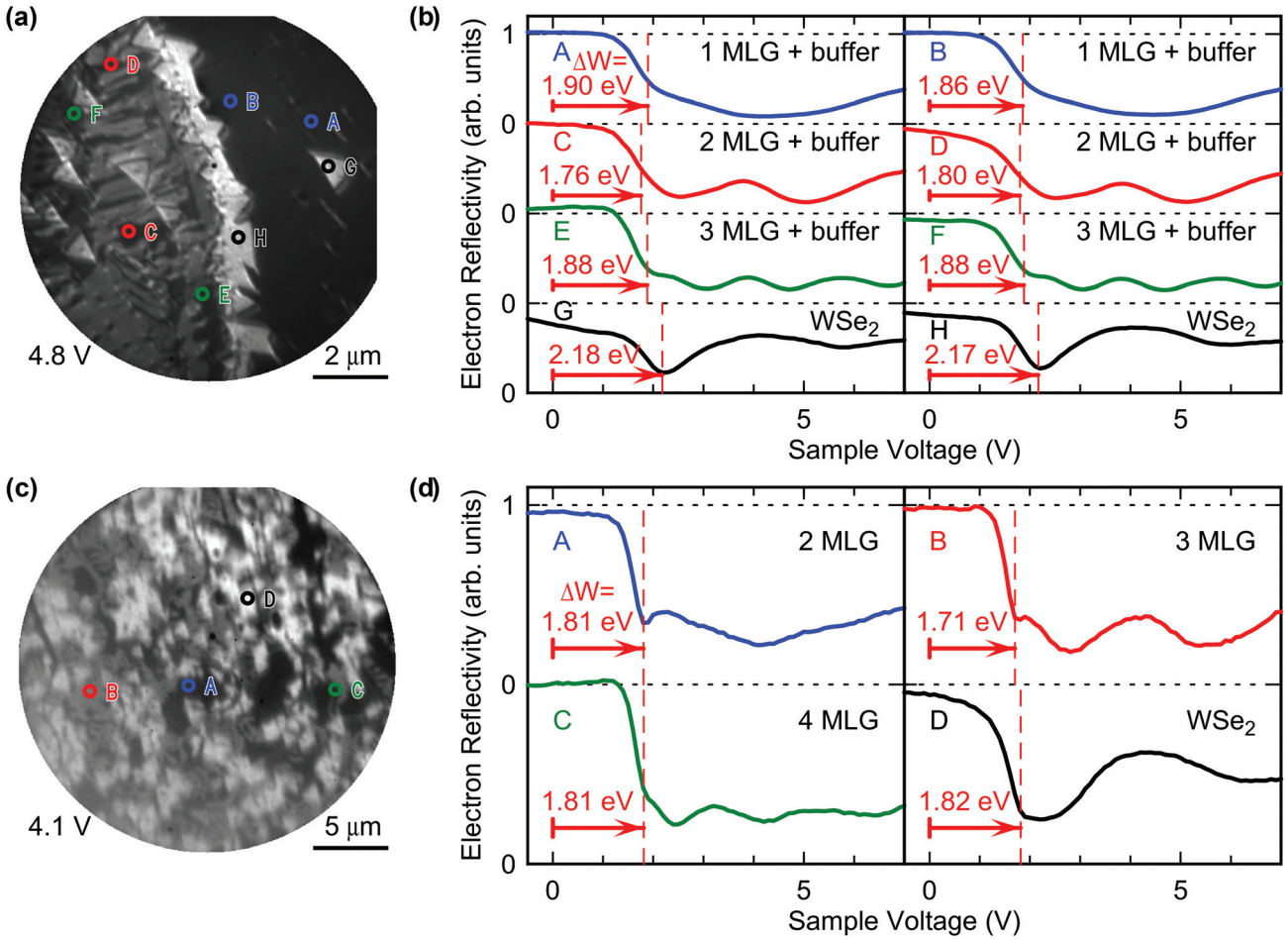

Fig. 3 (a) LEEM image of WSe_2 grown on EG-SiC at 800 °C (EG_{PH}), acquired at sample voltage of 6.2 V. Labeled points indicate location of reflectivity spectra in (b), which are used to identify the materials in the image. Bright triangles are WSe_2 islands, dark regions are mono- to multi-layers graphene on carbon-rich buffer layer. ΔW value, to the left of each spectrum in (b), quantify the electrostatic potential surface variation and hence the variation of the vacuum level. (c) LEEM image of WSe_2 grown on EG-SiC at 930 °C (EG_{FH}). (d) Reflectivity spectra of the points labeled in the (c); characteristic of a released buffer layer (due to passivated SiC dangling bonds). ΔW values show smaller variation than in the WSe_2–EG_{PH} case.

Low-energy electron reflectivity spectra (LEER) shows characteristic oscillations for graphene and WSe_2 for the respective regions of the surface and allow material identification in the LEEM images, as shown in Fig. 3b for the 800 °C WSe_2 growth.[28] Such LEER curves also permit determination of the local work function on the surface, since for sufficiently low sample voltages (~2 V) the incident electrons are totally reflected from the sample, *i.e.* the so-called "mirror-mode" transition. This voltage of this mirror-mode transition corresponds to the work function difference, ΔW, between the sample surface and the LEEM electron emitter. Detailed fitting of these transition voltages (energies) permits the extraction of the variation in work function across the surface.[2] A difference of eV is found between the work functions of monolayer graphene and WSe_2 on the sample surface (uncertainty from a combination of uncertainties in the measurement, analysis, and variations of the sample surface). It should be noted that this observed work function difference is between WSe_2 in contact with underlying graphene (G in the Fig. 3a) and a bare graphene region without WSe_2 covering the top (A or B in the Fig. 3a). The presence of interface dipoles and a change in local work function implies charge transfer between the WSe_2 and the graphene below. Consistent with this interpretation, it is noted that LEER curves measured on the WSe_2 islands from 800 °C growth (Fig. 3b) display a broad, sloping feature for voltages below the mirror-mode transition. This feature also indicates the presence of charge, or more specifically, electric dipoles on the edges of the triangular crystals which displace the incident and reflected electron beam during measurement, thus reducing the reflected intensity.[27]

The WSe_2–EG from the 930 °C WSe_2 growth shows similar 1 μm triangle islands of WSe_2 on an EG surface in LEEM (Fig. 3c), however, the sloping features in reflectivity associated with charge accumulations are much smaller than in the sample from the 800 °C WSe_2 growth. In addition, the extracted work function differences between uncovered bilayer graphene and WSe_2 (in contact) in the sample from 930 °C WSe_2 growth are negligible (0.03 ± 0.03 eV) compared to the

one grown at 800 °C, suggesting limited charge transfer between the layers after growth of WSe_2 (Fig. 3d). These observations, along with the presence of an additional, small minimum valley near 0 eV in the reflectivity spectra near the mirror-mode transition,[17] are attributed to full hydrogenation of the SiC surface, which passivates bonds between the carbon-rich buffer layer and the SiC.

This has the effect of releasing the buffer layer and increasing the count of freestanding graphene layers in the hydrogenated regions by 1, or creating quasi-freestanding-epitaxial graphene (QFEG), which is situated on H-terminated SiC.[19] Based on the evolution of graphene Raman spectra (Fig. 2b–d) and the LEEM/LEER investigation (Fig. 3), we conclude that the WSe_2 growth at high temperatures (>900 °C) leads to hydrogen intercalation and formation of fully hydrogenated (EG_{FH}) compared to those partially hydrogenated EG (EG_{PH}) at intermediate temperatures (750 °C to 850 °C), Fig. 1b.[17,19] Concurrently, the electrical properties of the WSe_2/EG interface appears to have significantly changed.

Conductive AFM *I–V* characteristics and band alignment model

The hydrogenation process is known to have a significant impact on the electrical properties of graphene on SiC. EG residing on top of the buffer layer on 6H-SiC (0001) is n-type doped[18,19,29] due to the combination of bulk and interface donor states[25,30] and has a Fermi energy 0.45 eV above the Dirac point.[25] In contrast, QFEG is known to be p-type doped.[17,25] This change has been explained by the presence of the spontaneous polarization of the hexagonal 6H-SiC substrate, which lowers the Fermi energy to a position 0.28–0.30 eV below the Dirac point for complete hydrogenation.[25,31] This modification in the doping of graphene can thereby influence the electrical transport properties across the WSe_2–graphene interface on SiC. In order to elucidate the transport properties, vertical current *versus* voltage (*I–V*) measurements were performed on the 800 °C and 930 °C WSe_2 growth (labeled as WSe_2–EG_{PH} and WSe_2–EG_{FH}, respectively) in Conductive AFM (CAFM).

A CAFM tip with PtIr coating, and the graphene, serves as source and drain, respectively. While the WSe_2–EG_{PH} diode exhibits a *I–V* with turn-on current at bias of ≥1 V; however, the WSe_2–EG_{FH} diode turns on near zero bias (Fig. 4a and S2a–2c†). The main component of the CAFM current near zero bias for WSe_2–EG_{PH} is due to tunneling from the CAFM tip to graphene through the WSe_2 gap. On the other hand, For WSe_2–EG_{FH}, the WSe_2 layer acts as a short between the CAFM tip and the EG_{FH} (Fig. 4b).

Our LEEM measurements and analysis above indicate a work function difference of 0.31 eV between the WSe_2 (in

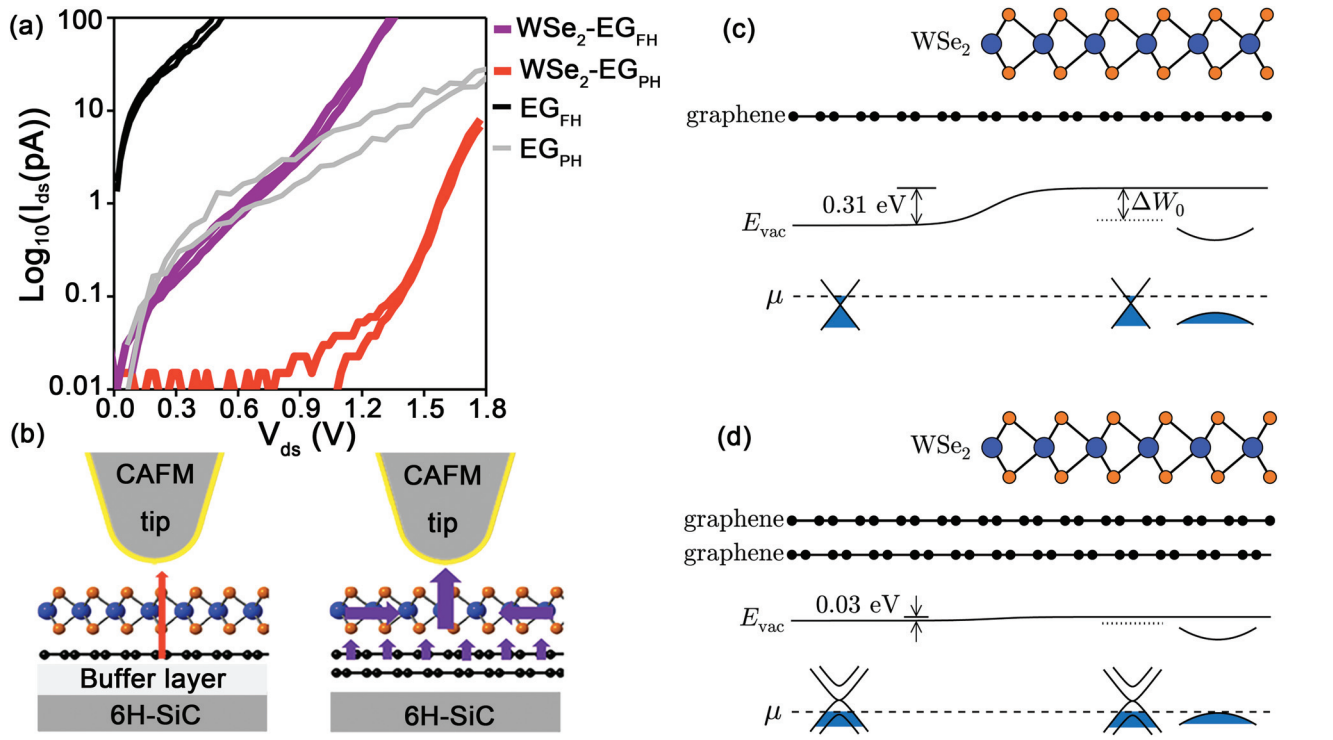

Fig. 4 Electrical measurements (a) show that the *I–V* of EG_{PH}, EG_{FH}, WSe_2–EG_{PH}, and WSe_2–EG_{FH}. WSe_2–EG_{PH} is more resistive than that of WSe_2–EG_{FH}, indicating the barrier to transport is larger for WSe_2–EG_{PH}. (b) The WSe_2–EG_{PH} resulted in a small tunneling current (left), while the tunneling current is magnified after the decoupling of buffer layer (right). The yellow surface of CAFM tips symbols PtIr coatings. Band alignment and vacuum energy diagrams for the two heterostructures, WSe_2–EG_{PH} (c) and WSe_2–EG_{FH} (d), showing variations of vacuum energy of the surface due to partial WSe_2 coverage.

contact with EG_{PH}) and the uncovered monolayer EG_{PH}, while the work function difference between the WSe_2 (in contact with EG_{FH}) and the uncovered bilayer EG_{FH} is near zero. The measured work function difference is a combination effect of intrinsic interface dipole and extrinsic interface dipole. The extrinsic dipole is due to doping caused by charge transfer between WSe_2 and graphene. The intrinsic dipole results from redistribution of charge within the WSe_2 or graphene itself upon contact. In other words, it is the difference between vacuum level of undoped WSe_2 and that of undoped graphene when they are put in contact. Density functional theory (DFT) calculations of this intrinsic dipole are performed using the Vienna *ab initio* simulation package (VASP)[32] with the projector-augmented wave (PAW) method.[33] The local density approximation (LDA)[34] is used to describe the exchange–correlation functional with the partial core correction included. More DFT calculation details are provided in the ESI.† As shown in Fig. S3,† the vacuum energy level above WSe_2 is 0.17 eV higher than that above graphene, indicating an (intrinsic) dipole from graphene towards the WSe_2.

Using this intrinsic dipole, along with the measured work function differences, we propose a model in which the WSe_2 has some unintentional p-type doping, and transfer of charge between the EG_{PH} or EG_{FH} and the WSe_2 (combined with the intrinsic dipole) produces the observed variation in work function. With knowledge of the doping density of EG_{PH} and EG_{FH} ($(4 \pm 1) \times 10^{12}$ cm^{-2} n-type and $(1.5 \pm 0.2) \times 10^{13}$ cm^{-2} p-type, respectively, from our previous electrical studies on EG_{PH} and EG_{FH}),[19,35] and using reported values of electron affinities of monolayer graphene (4.57 eV) and bilayer graphene (4.71 eV),[36] we compute the transfer of charge between the WSe_2 and the EG_{PH} or EG_{FH}. This charge transfer, for a given (unintentional) doping density of the WSe_2, yields theoretical values for the work function differences; the doping density is determined by matching these differences to experiment. Our model is illustrated in Fig. 4c and d. The dependence of the results on the electron affinities of graphene is discussed in ESI.†

For the charge transfer computation, we employ the standard linear band structure around the *K* point for the monolayer graphene from EG_{PH}, and hyperbolic bands near the band extrema for bilayer graphene from EG_{FH} and for WSe_2 around *K* points, based on tight-binding models.[37,38] The method to compute the electrostatics is similar to that described by Li *et al.*[39] Fig. 4c and d show band diagrams of the WSe_2–EG_{PH} and WSe_2–EG_{FH} surfaces, which are graphene partially covered by WSe_2. Both the intrinsic interface dipole and the charge transfer are taken into account and equilibrium is reached when the Fermi levels are aligned. The difference between the vacuum energy of WSe_2 (in contact with graphene) and the underlying graphene (*e.g.* ΔW_0 in Fig. 4c) is thus a sum of the intrinsic interface dipole effect and the charge transfer effect.

In order to match the theoretical work function difference between the WSe_2 (in contact) and the uncovered graphene with the experimental values (0.31 eV and 0.03 eV for WSe_2–EG_{PH} and WSe_2–EG_{FH} respectively), we employ an unintentional p-type doping of 1.3×10^{12} cm^2 for the WSe_2 before charge transfer between the WSe_2 and the underlying graphene. When the WSe_2 is put in contact with EG_{PH} (n-type), electrons transfer from the EG_{PH} to the WSe_2, leading to nearly complete compensation of the p-type doping in the WSe_2 and a negligible carrier density in the WSe_2. The Fermi level ends up well inside the bandgap of the WSe_2 and near the charge neutrality point in the graphene (Fig. 4c). For the case of the WSe_2 in contact with the EG_{FH} (p-type), electrons transfer from the WSe_2 to the EG_{FH}, making the WSe_2 more p-type (carrier density 2.9×10^{12} cm^{-2}). The resulting Fermi level of the WSe_2–EG_{FH} remains near the top of the valence band of its WSe_2. In other words, the WSe_2 on the EG_{PH} forms a Schottky barrier (*i.e.* relatively low conductivity), whereas the WSe_2 on the EG_{FH} forms as ohmic contact (*i.e.* high conductivity), and leading to a $\sim 10^3\times$ increase in current drive (Fig. 4a).

An additional output of our charge transfer computations is the sum of the bandgap plus electron affinity of the WSe_2, $\chi_{WSe_2} + E_g$ (only the sum enters, since the electron density in the WSe_2 conduction band is negligible). In order to match the observed work function variations, we deduce an unintentional doping density in the WSe_2 of 1.3×10^{12} cm^{-2}, and the value of $^{\chi}{}_{WSe2} + E_g$ is determined to be 5.1 eV. This value is consistent with a recently reported electron affinity of ~3.1 eV for WSe_2 using first-principles GW calculation,[40] together with a bandgap of ~2 eV, which is in agreement with several recently reported experimental values.[41,42] Variation of our deduced values due to uncertainty in the other parameters in the problem is discussed in the ESI.†

Conclusions

By varying the temperatures for growth of WSe_2 on EG in a pure H_2 environment, the transport across WSe_2–Graphene heterostructures is controllable. The investigation combining LEED/LEEM, Raman spectra, and electrical measurements on the heterostructures confirmed the transport across the interface is controlled by the doping of the EG, which in turn is tuned by the presence of a carbon buffer. The band alignment diagrams of two different heterostructures were constructed with the measured work function difference between the WSe_2 and the graphene from LEER. Taking into account their intrinsic interface dipoles and charge transfer, the diagrams show the presence of the Schottky barrier in WSe_2–EG_{PH} and a reduced barrier in WSe_2–EG_{FH}, which are in agreement with their *I*–*V* characteristics.

The work described here is foundational for understanding vertical transport in graphene-based 2D heterostructures, demonstrating that doping of the graphene plays a critical role in these novel structures. Epitaxial graphene is unique because it can be made n- or p-type based on the TMD growth conditions, allowing for one to readily engineer the transport between graphene and to n- or p-type TMDs with a truly pristine interface.

Author contributions

J. A. R. and Y.-C. L. conceived the idea, and J. A. R., R. M. F., K. C., and R. M. W. directed the research. Y.-C. L. and S. M. E. synthesized vdW heterostructures; Y.-C. L. carried out AFM, Raman, PL and electrical measurements; S. C. dlB. and P. C. M. performed LEED/LEER; J. Li proposed band alignment models combining LEED and electrical measurement data; Y. N. carried out DFT calculations for interface dipoles between WSe_2 and graphene; R. A. carried out XPS and compared XPS results with previous works. All authors discussed the results. Y.-C. L. and J. A. R. wrote the paper with significant input from J. L., S. C. dlB., and R. M. F. All authors have read and approved the manuscript.

Acknowledgements

Support is acknowledged by the Center for Low Energy Systems Technology (LEAST), one of six centers supported by the STARnet phase of the Focus Center Research Program (FCRP), a Semiconductor Research Corporation program sponsored by MARCO and DARPA. The WiteC Raman system and Bruker Dimension AFM, and nanofabrication facilities were supported by the National Nanotechnology Infrastructure Network at the Penn State. We thank Shruti Subramanian (MatSE, Penn State) for her assistance on epitaxial graphene synthesis. We also acknowledge Christopher Smyth (MatSE, UT Dallas) for his assistance on XPS data analysis.

References

1 M. Chhowalla, Z. Liu and H. Zhang, *Chem. Soc. Rev.*, 2015, **44**, 2584–2586.
2 G. R. Bhimanapati, Z. Lin, V. Meunier, Y. Jung, J. J. Cha, S. Das, D. Xiao, Y. Son, M. S. Strano, V. R. Cooper, L. Liang, S. G. Louie, E. Ringe, W. Zhou, B. G. Sumpter, H. Terrones, F. Xia, Y. Wang, J. Zhu, D. Akinwande, N. Alem, J. A. Schuller, R. E. Schaak, M. Terrones and J. A. Robinson, *ACS Nano*, 2015, **9**, 11509–11539.
3 A. K. Geim and I. V. Grigorieva, *Nature*, 2013, **499**, 419–425.
4 C. Tan and H. Zhang, *J. Am. Chem. Soc.*, 2015, **137**, 12162–12174.
5 T. Georgiou, R. Jalil, B. D. Belle, L. Britnell, R. V. Gorbachev, S. V. Morozov, Y.-J. Kim, A. Gholinia, S. J. Haigh, O. Makarovsky, L. Eaves, L. A. Ponomarenko, A. K. Geim, K. S. Novoselov and A. Mishchenko, *Nat. Nanotechnol.*, 2013, **8**, 100–103.
6 W. J. Yu, Y. Liu, H. Zhou, A. Yin, Z. Li, Y. Huang and X. Duan, *Nat. Nanotechnol.*, 2013, **8**, 952–958.
7 K. Roy, M. Padmanabhan, S. Goswami, T. P. Sai, G. Ramalingam, S. Raghavan and A. Ghosh, *Nat. Nanotechnol.*, 2013, **8**, 826–830.
8 S. J. Haigh, A. Gholinia, R. Jalil, S. Romani, L. Britnell, D. C. Elias, K. S. Novoselov, L. A. Ponomarenko, A. K. Geim and R. Gorbachev, *Nat. Mater.*, 2012, **11**, 764–767.
9 Y. Shi, H. Li and L.-J. Li, *Chem. Soc. Rev.*, 2015, **44**, 2744–2756.
10 Y.-C. Lin, N. Lu, N. Perea-Lopez, J. Li, Z. Lin, X. Peng, C. H. Lee, C. Sun, L. Calderin, P. N. Browning, M. S. Bresnehan, M. J. Kim, T. S. Mayer, M. Terrones and J. A. Robinson, *ACS Nano*, 2014, **8**, 3715–3723.
11 Y.-C. Lin, C.-Y. S. Chang, R. K. Ghosh, J. Li, H. Zhu, R. Addou, B. Diaconescu, T. Ohta, X. Peng, N. Lu, M. J. Kim, J. T. Robinson, R. M. Wallace, T. S. Mayer, S. Datta, L.-J. Li and J. A. Robinson, *Nano Lett.*, 2014, **14**, 6936–6941.
12 Y.-C. Lin, R. K. Ghosh, R. Addou, N. Lu, S. M. Eichfeld, H. Zhu, M.-Y. Li, X. Peng, M. J. Kim, L.-J. Li, R. M. Wallace, S. Datta and J. A. Robinson, *Nat. Commun.*, 2015, **6**, 7311.
13 X. Li, L. Basile, B. Huang, C. Ma, J. Lee, I. V. Vlassiouk, A. A. Puretzky, M.-W. Lin, M. Yoon, M. Chi, J. C. Idrobo, C. M. Rouleau, B. G. Sumpter, D. B. Geohegan and K. Xiao, *ACS Nano*, 2015, **9**, 8078–8088.
14 S. J. Kim, K. Choi, B. Lee, Y. Kim and B. H. Hong, *Annu. Rev. Mater. Res.*, 2015, **45**, 63–84.
15 D. Qu, X. Liu, F. Ahmed, D. Lee and W. J. Yoo, *Nanoscale*, 2015, **7**, 19273–19281.
16 S. M. Eichfeld, L. Hossain, Y.-C. Lin, A. F. Piasecki, B. Kupp, A. G. Birdwell, R. A. Burke, N. Lu, X. Peng, J. Li, A. Azcatl, S. McDonnell, R. M. Wallace, M. J. Kim, T. S. Mayer, J. M. Redwing and J. A. Robinson, *ACS Nano*, 2015, **9**, 2080–2087.
17 C. Riedl, C. Coletti, T. Iwasaki, A. A. Zakharov and U. Starke, *Phys. Rev. Lett.*, 2009, **103**, 246804.
18 K. V. Emtsev, A. Bostwick, K. Horn, J. Jobst, G. L. Kellogg, L. Ley, J. L. McChesney, T. Ohta, S. A. Reshanov, J. Röhrl, E. Rotenberg, A. K. Schmid, D. Waldmann, H. B. Weber and T. Seyller, *Nat. Mater.*, 2009, **8**, 203–207.
19 J. A. Robinson, M. Hollander, M. Labella, K. A. Trumbull, R. Cavalero and D. W. Snyder, *Nano Lett.*, 2011, **11**, 3875–3880.
20 A. Koma, *Thin Solid Films*, 1992, **216**, 72–76.
21 H. Terrones, E. Del Corro, S. Feng, J. M. Poumirol, D. Rhodes, D. Smirnov, N. R. Pradhan, Z. Lin, M. A. T. Nguyen, A. L. Elías, T. E. Mallouk, L. Balicas, M. A. Pimenta and M. Terrones, *Sci. Rep.*, 2014, **4**, 4215.
22 A. C. Ferrari, *Solid State Commun.*, 2007, **143**, 47–57.
23 J. A. Robinson, C. P. Puls, N. E. Staley, J. P. Stitt and M. A. Fanton, *Nano Lett.*, 2009, **9**, 964–968.
24 A. Das, S. Pisana, B. Chakraborty, S. Piscanec, S. K. Saha, U. V. Waghmare, K. S. Novoselov, H. R. Krishnamurthy, A. K. Geim, A. C. Ferrari and A. K. Sood, *Nat. Nanotechnol.*, 2008, **3**, 210–215.
25 J. Ristein, S. Mammadov and T. Seyller, *Phys. Rev. Lett.*, 2012, **108**, 246104.
26 R. M. Feenstra, N. Srivastava, Q. Gao, M. Widom, B. Diaconescu, T. Ohta, G. L. Kellogg, J. T. Robinson and

I. V. Vlassiouk, *Phys. Rev. B: Condens. Matter*, 2013, **87**, 041406.
27 D. P. Gopalan, P. C. Mende, S. C. de la Barrera, S. Dhingra, J. Li, K. Zhang, N. A. Simonson, J. A. Robinson, N. Lu, Q. Wang, M. J. Kim, B. D'Urso and R. M. Feenstra, *J. Mater. Res.*, 2016, **31**, 7.
28 S. Vishwanath, X. Liu, S. Rouvimov, P. C. Mende, A. Azcatl, S. McDonnell, R. M. Wallace, R. M. Feenstra, J. K. Furdyna, D. Jena and H. Grace Xing, *2D Mater.*, 2015, **2**, 024007.
29 T. Ohta, A. Bostwick, J. L. McChesney, T. Seyller, K. Horn and E. Rotenberg, *Phys. Rev. Lett.*, 2007, **98**, 206802.
30 S. Kopylov, A. Tzalenchuk, S. Kubatkin and V. I. Fal'ko, *Appl. Phys. Lett.*, 2010, **97**, 112109.
31 S. Mammadov, J. Ristein, R. J. Koch, M. Ostler, C. Raidel, M. Wanke, R. Vasiliauskas, R. Yakimova and T. Seyller, *2D Mater.*, 2014, **1**, 035003.
32 G. Kresse and J. Furthmüller, *Phys. Rev. B: Condens. Matter*, 1996, **54**, 11169–11186.
33 G. Kresse and D. Joubert, *Phys. Rev. B: Condens. Matter*, 1999, **59**, 1758–1775.
34 D. M. Ceperley and B. J. Alder, *Phys. Rev. Lett.*, 1980, **45**, 566–569.
35 M. J. Hollander, A. Agrawal, M. S. Bresnehan, M. LaBella, K. A. Trumbull, R. Cavalero, D. W. Snyder, S. Datta and J. A. Robinson, *Phys. Status Solidi*, 2013, **210**, 1062–1070.
36 Y.-J. Yu, Y. Zhao, S. Ryu, L. E. Brus, K. S. Kim and P. Kim, *Nano Lett.*, 2009, **9**, 3430–3434.
37 G.-B. Liu, W.-Y. Shan, Y. Yao, W. Yao and D. Xiao, *Phys. Rev. B: Condens. Matter*, 2013, **88**, 085433.
38 E. McCann and M. Koshino, *Rep. Prog. Phys.*, 2013, **76**, 056503.
39 M. (Oscar) Li, D. Esseni, G. Snider, D. Jena and H. Grace Xing, *J. Appl. Phys.*, 2014, **115**, 074508.
40 Y. Liang, S. Huang, R. Soklaski and L. Yang, *Appl. Phys. Lett.*, 2013, **103**, 042106.
41 K. He, N. Kumar, L. Zhao, Z. Wang, K. F. Mak, H. Zhao and J. Shan, *Phys. Rev. Lett.*, 2014, **113**, 026803.
42 C. Zhang, Y. Chen, A. Johnson, M.-Y. Li, L.-J. Li, P. C. Mende, R. M. Feenstra and C.-K. Shih, *Nano Lett.*, 2015, **15**, 6494–6500.